Unveiling Single Atom Nucleation for Isolating Ultrafine fcc Ru Nanoclusters with Outstanding Dehydrogenation Activity

Ye Wang, Jia-Luo Li, Wen-Xiong Shi, Zhi-Ming Zhang, Song Guo, Rui Si,* Meng Liu, Hong-Cai Zhou,* Shuang Yao, Chang-Hua An, and Tong-Bu Lu**

Ultrafine face-centered cubic (fcc) ruthenium nanoclusters (NCs) are of great interest due to their super high catalytic activity. However, it is extremely difficult to prepare ≈1 nm fcc ruthenium NCs with high energy atoms due to their easy aggregation. Herein, the nucleation process of ruthenium centers by confined pyrolysis of a multivariate metal–organic framework to isolate ultrafine fcc NCs (from single atom to 1.33 nm) via in situ formed stabilizers is unveiled. Systematic investigations demonstrate that preferential nucleation of Ru single atoms to fcc clusters in the initial nucleation represents a key step and makes it possible to separate ultrafine fcc Ru NCs with in situ formed N-doped porous carbon. A record high turnover frequency of 1300.53 min^{-1} for methanolysis of ammonia borane is achieved by 1.33 nm NCs. This work suggests a new strategy to prepare ultrafine metal NCs by instantly capturing structure-specific crystal nuclei with in situ formed stabilizers.

1. Introduction

Unveiling the nucleation process for controlling aggregation of metal cations into structure-specific crystal nuclei represents a key step for isolating ultrafine nanoclusters (NCs) with advanced functionality.[1–6] In liquid phase, metal cation nucleation into ultrafine crystal nuclei represents an essential step in the crystallization of nanomaterials. These ultrafine clusters have been regarded as key intermediates during self-catalyzed crystal growth,[7–9] which have played a decisive role in the precise control of the size and structure of the final products. As a result, ingenious control of nucleation conditions can create various nanomaterials with prominent size and geometry-dependent functionality.[10–16] However, it is still a great challenge to isolate ultrafine NCs in liquid phase because the crystal nuclei are extremely prone to aggregation without the stabilizers in the initial nucleation process.

Ru metal tends to adopt hexagonal close packed (hcp) structures with low potential energy in the bulk phase at all temperature ranges.[17–19] Recently, more attention has been paid to explore Ru nanoparticles (NPs) in face-centered cubic (fcc) phase with more exposed active sites than their hcp analogue.[20] They usually exhibit much higher catalytic activity than that of hcp Ru NPs in a number of reactions, such as methanol oxidation, hydrogenation, Fischer–Tropsch synthesis, and dehydrogenation, especially for ammonia borane (AB) methanolysis.[21–30] Recently, controlled synthesis of ultrafine fcc Ru NCs has been of significant interest to further greatly improve their catalytic efficiency.[28,29] Up to date, fcc Ru NPs with sizes > 2.0 nm have been confirmed by theoretical and experimental investigations. For example, fcc Pt NPs were applied as core for epitaxial growth to form 6.8 ± 1.5 nm fcc Ru NPs with polyvinylpyrrolidone as a weak stabilizer.[27] In another case, pure fcc Ru NPs with a diameter of 2–5.5 nm were synthesized via a chemical reduction method with γ-Al$_2$O$_3$ as the support.[28] Most recently, Zhou and co-workers designed a negatively charged porous coordination cages as a template for the synthesis of ultrafine fcc Ru NCs with an average size of 2.5 nm. This particular work exhibits a record high turnover frequency (TOF) of 304.4 min^{-1} in AB methanolysis.[29] These small fcc Ru NPs are all confirmed as high-performance catalysts due to the exposure of high energy crystal plane. They were all obtained

---

Y. Wang, Dr. W.-X. Shi, Prof. Z.-M. Zhang, Dr. S. Guo, Dr. M. Liu,
Dr. S. Yao, Prof. C.-H. An, Prof. T.-B. Lu
Institute for New Energy Materials & Low Carbon Technologies
School of Materials Science & Engineering
School of Chemistry and Chemical Engineering
Tianjin University of Technology
Tianjin 300384, China
E-mail: zmzhang@email.tjut.edu.cn; lutongbu@email.tjut.edu.cn

Dr. J.-L. Li, Prof. H.-C. Zhou
Department of Chemistry
Texas A&M University
College Station, TX 77843-3255, USA
E-mail: zhou@chem.tamu.edu

Dr. W.-X. Shi
School of Materials Science and Engineering
State Key Laboratory of Separation Membranes
and Membrane Processes
Tiangong University
Tianjin 300387, China

Prof. R. Si
Shanghai Synchrotron Radiation Facility
Zhangjiang Laboratory
Shanghai 201204, China
E-mail: sirui@sinap.ac.cn

The ORCID identification number(s) for the author(s) of this article can be found under https://doi.org/10.1002/aenm.202002138.

DOI: 10.1002/aenm.202002138

through carefully and ingeniously designed synthesis strategy. Further reducing the size of fcc Ru NPs into ultrafine fcc Ru NCs around 1 nm will make them contain higher energy atoms to give them a very high catalytic activity. It is no doubt that this will be one of the best strategies to optimize advanced materials for high-performance catalysis. However, no effective strategy has been explored to achieve ≈1 nm fcc Ru NCs.

For the synthesis of ultrafine NCs, heterogeneous porous supports, homogeneous templates, and solution phase surfactants have been applied as stabilizers.[31–34] In these studies, strong metal–support interaction was considered as an efficient strategy to stabilize high surface-energy single-site catalysts and ultrafine NCs.[35–40] Among them, metal–organic frameworks (MOFs) were investigated intensively due to their tunable structure, composition, and internal cavities. These advantages made this candidate ideal for ordered and tunable confinement of metal atoms/clusters, preventing excessive agglomeration during the catalytic processes.[4,41–45] However, large metal NPs are often formed in the pyrolysis process due to the fast aggregation of high-energy metal centers during the destruction of the MOF templates. It is well known that MOFs can act as molecular platform to incorporate mixed-ligands or mixed-metal centers into a crystalline framework, giving rise to multivariate (MTV) MOFs as the solid solution.[46–48] The proportions of the mixed-ligand or mixed-metal can be easily adjusted in the MTV MOFs to control the concentration of the solid solution. In this pyrolysis process, the organic components and their decomposed fragments can act simultaneously as the reductants and stabilizers via the in situ formation of N-doped porous carbon (NDPC), which can be used to stabilize the resulting metal NCs. Similar to NC nucleation in liquid-phase systems, the aggregation and nucleation of these metal centers should happen during the pyrolysis of the solid solution. Therefore, mimicking the liquid-phase crystal growth process, instantly capturing crystal nucleus with in situ formed stabilizers during the initial nucleation process should represent an effective synthetic strategy to synthesize ultrafine NCs. However, isolating ultrafine fcc Ru NCs around 1 nm has still represents a great challenge due to the unclear nucleation mechanism makes it extremely difficult to determine the nucleation stage of fcc Ru NCs.

In this work, we adopted a MTV synthetic strategy to uniformly disperse ruthenium centers into a porous UiO-67 framework through a one-pot reaction of Ru–L/H_2bpdc (Ru-L = $[Ru(bpy)_2(H_2bpydc)]^{2+}$, bpy = 2,2′-Bipyridine, H_2bpydc = 2,2′-Bipyridine-5,5′-dicarboxylic acid, H_2bpdc = Biphenyl-4,4′-dicarboxylic acid) with Zr^{4+}, constructing a MTV MOF as the solid solution. Systematic experimental investigation and simulated nucleation demonstrates that Ru centers tend to preferentially aggregate from single atoms (SAs) to ultrafine fcc NCs during the initial aggregation stage, thus providing the possibility for immobilizing ultrafine fcc Ru NCs into the in situ formed NDPC. As a result, for the first time, a series of uniform Ru fcc NCs with the size around 1 nm (0.93, 1.15, and 1.33 nm) were controllably synthesized via the variation of the pyrolysis temperature and ruthenium concentration of the MTV MOF. Further, a transformation of fcc Ru NCs to hcp NCs (2.16 nm) with lower energy atoms was achieved during the aggregation process of Ru SAs via further increasing the Ru concentration. Impressively, 1.33 nm fcc Ru NCs exhibit remarkable catalytic activity for the methanolysis of AB with a record-high TOF of 1300.53 min^{-1}.

2. Results and Discussion

2.1. Synthesis and Characterization

The heterogeneous Ru-based SA and NC catalysts were prepared via the pyrolysis of MTV MOF (**Figure 1**a). First, the MTV

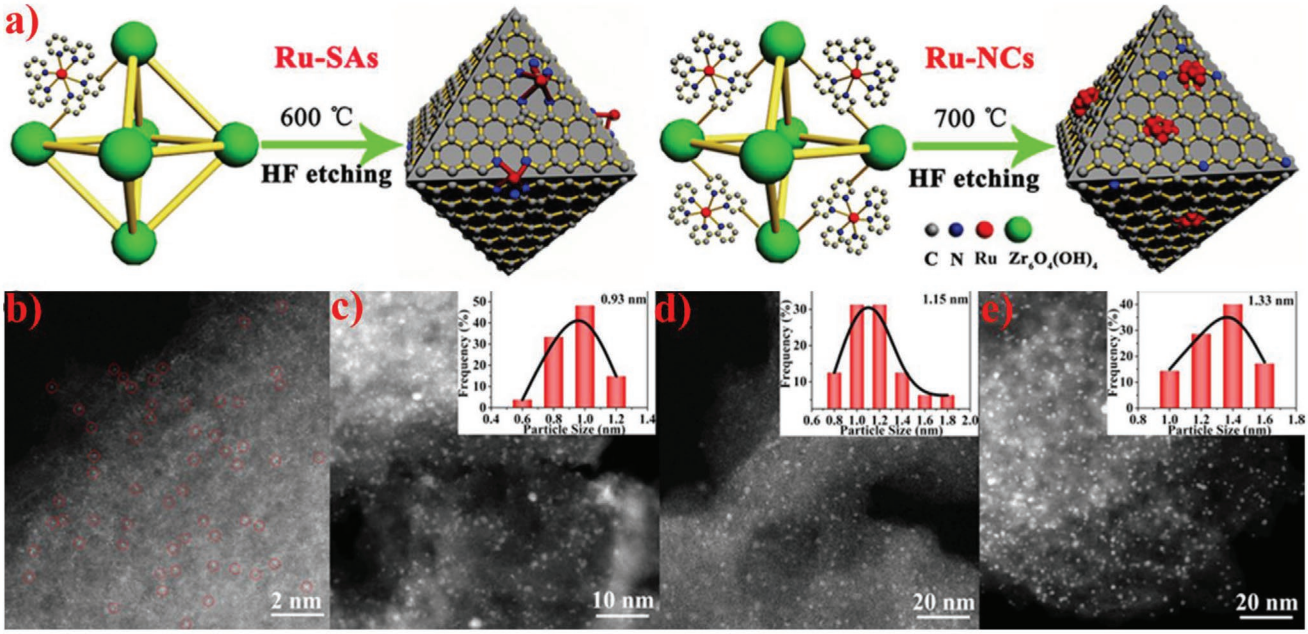

Figure 1. a) Scheme view of the synthetic procedure for Ru-1–4, HADDF-STEM images of b) SA catalyst of Ru-1a, SAs are highlighted with red circles, c) Ru-1b, d) Ru-2, and e) Ru-3.

MOFs were directly synthesized with a mix-and-match synthetic strategy by a one pot reaction of $ZrCl_4$, 2,2′-bipyridine-5,5′-dicarboxylic acid (H_2bpdc), and Ru(bpy)$_2$(H_2bpydc) (Ru–L) (Figures S1 and S2, Supporting Information). During this crystallization process, the Ru cations were evenly dispersed over the crystalline UiO-67 framework. In this MTV MOF, the concentration of Ru metal centers could be easily controlled and adjusted by tuning the loading molar ratio of H_2bpdc/Ru–L. As shown in Figure S3 (Supporting Information), the color of the reaction solution gradually darkened proportionally to the concentration of Ru–L. A series of Ru–MOFs (Ru–MOF-1–4) was obtained with molar ratios of H_2bpdc to Ru–L of 40: 1, 30: 1, 10: 1, and 5: 1, respectively. Scanning electron microscopy (SEM) images show that the Ru–MOFs exhibit the typical octahedral morphology of UiO-67 with the size mainly between 100 and 300 nm. Elemental mapping results reveal that the Ru is uniformly dispersed on the crystalline octahedra (Figures S4 and S5, Supporting Information). The powder X-ray diffraction (PXRD) patterns of these MTV MOFs are similar to that of simulated results, indicating that these Ru–MOFs indeed maintain the structure and shape of the parent UiO-67 (Figure S6, Supporting Information).

To demonstrate the nucleation of the Ru centers in the MTV MOF, MOFs with different loading amounts of Ru were thermally treated in an argon atmosphere at variable temperatures to control the nucleation rate of the NCs. After a 3 h pyrolysis at 600 and 700 °C, the skeleton of the Ru–MOFs was in situ transformed into NDPC, decorated by small ZrO_2 nanocrystals and Ru species (Figure S7, Supporting Information). Element Zr was removed from the NDPC by hydrofluoric (HF) treatment, eliminating the possibility of the interference of Zr in the high-resolution TEM (HRTEM) test. The final products derived from Ru–MOF-1 obtained by pyrolysis at 600 and 700 °C were named as Ru-1a and Ru-1b, respectively. The products from Ru–MOF-2–4 obtained by pyrolysis at 700 °C were named Ru-2, Ru-3, and Ru-4, respectively. The loading amounts of Ru for these products were determined to be 0.17%, 0.29%, 0.57%, 2.40%, and 4.01%, respectively by inductively coupled plasma-mass spectrometry (ICP-MS). To further conform the Ru contents in the samples, we conducted energy dispersive X-ray spectroscopy (EDS) analysis on HRTEM. The EDS data showed that the Ru wt% of Ru-1a, Ru-1b, Ru-2, Ru-3, Ru-4 are 0.28, 0.45, 0.60, 3.26, 4.79, respectively. The EDS results also reveal that the Ru contents are very low in these samples, confirming the rationality of the ICP results (Figures S8 and S9, Supporting Information). Further, ICP-MS analysis and EDS results reveal that trace amount of Zr element remains in these samples (Figures S8, S9, and Table S1, Supporting Information), however the Zr species did not have obvious influence on the catalytic performance (detail discussion was supplied in the catalytic section).

SEM measurements were performed on the pyrolysis products to reveal their morphology and size. As shown in Figure S10 (Supporting Information), the pyrolysis products show initial octahedral structure of the pristine MOF nanocrystals. Further, aberration-corrected high angle annular dark field scanning transmission electron microscopy (HAADF-STEM) was performed on these samples to track the aggregation process via regulating the pyrolysis temperatures and Ru concentrations. For Ru-1a calcined at 600 °C, high density bright dots can be observed in the NDPC support, indicating the formation of SA Ru on the stabilizer (Figure 1b). By increasing the pyrolysis temperature to 700 °C, the aggregation of SA Ru into 0.93 nm ultrafine NCs can be observed in the Ru-1b (Figure 1c). Intensity profile analysis of the HADDF-STEM results indicate the atomic distance of Ru in Ru-1a is around 0.45 nm, much longer than that in the nanocluster of Ru-1b of around 0.17 nm. These results further confirm the SA distribution of Ru center in Ru-1a, which is consistent with the extended X-ray absorption fine structure (EXAFS) results (Figure S11, Supporting Information). These SAs and NCs were stabilized by the NDPC, which was in situ formed in the pyrolysis of MTV MOF. These observations reveal that the strong MOF interactions with two additional bpy ligands as the space isolation agent can promote the formation of Ru SAs without the formation of Ru NCs at a lower pyrolysis temperature. By further increasing the pyrolysis temperature to 700 °C, this MOF interaction can be restrictively broken, thus the Ru SAs partially aggregated into ultrafine NCs. As shown in Figure S12 (Supporting Information), there are still abundant Ru SA centers on the NDPC support those coexist with the ultrafine Ru NCs in Ru-1b. Meanwhile, a similar nucleation behavior to that of what would be expected in a liquid solution was observed, where the size of NCs increased gradually with an increase in the Ru concentration.[8,9] Very interestingly, the in situ formed supports with strong immobilizing ability can ensure the effective capture and stabilization of ultrafine NCs. Thus, Ru–NCs with the sizes of 0.93, 1.15, 1.33, and 2.16 nm were facilely obtained by the pyrolysis of Ru–MOF-1–4 at the same temperature of 700 °C (Figure 1; and Figures S13–S16, Supporting Information). Control experiments were performed through the introduction of $RuCl_3$ in the samples instead of Ru–L incorporation with a similar loading amount of Ru (Ru–MOF-5). PXRD patterns indicated that Ru–MOF-5 containing Ru^{3+} still maintained the parent UiO-67 structure (Figure S17, Supporting Information). After the pyrolysis at 700 °C and HF etching, the loading amount of Ru was determined to be 0.38% by ICP-MS, and the product was named as Ru-5. As shown in Figure S18 (Supporting Information), obvious characteristic peaks of the Ru particles were observed in the PXRD of ZrO_2–Ru-5 and Ru-5, indicating the formation of large Ru-based NP occurs by replacing the MTV MOF with a mixture of pristine UiO-67 and $RuCl_3$. Therefore, the strong MOF interactions exhibited in the MTV MOF can be determined to efficiently control the NC nucleation rate and ensure the effective separation of the ultrafine NCs.

HAADF-STEM images and corresponding elemental mapping results show that the Ru, N, C, and O are all uniformly dispersed in the NDPC supports in the Ru-1a–4 samples (**Figure 2**; and Figures S13–S16, Supporting Information). The HRTEM images clearly show a fivefold-symmetry twinned NP, representing the (111) fcc planes with decahedral structure, which is well-known as a typical fcc structure of metal NPs (Figure 2d). As shown in Figures S19 and S20 (Supporting Information), the HRTEM and HAADF-STEM images of Ru-1b and Ru-2 also clearly show the lattice constants of ≈2.21 Å, corresponding to the lattice spacing of (111) fcc Ru NCs. These results were further confirmed by the fast Fourier transform (FFT) diffraction pattern, which unambiguously illustrated a typical fcc structure of these metal NCs.[49]

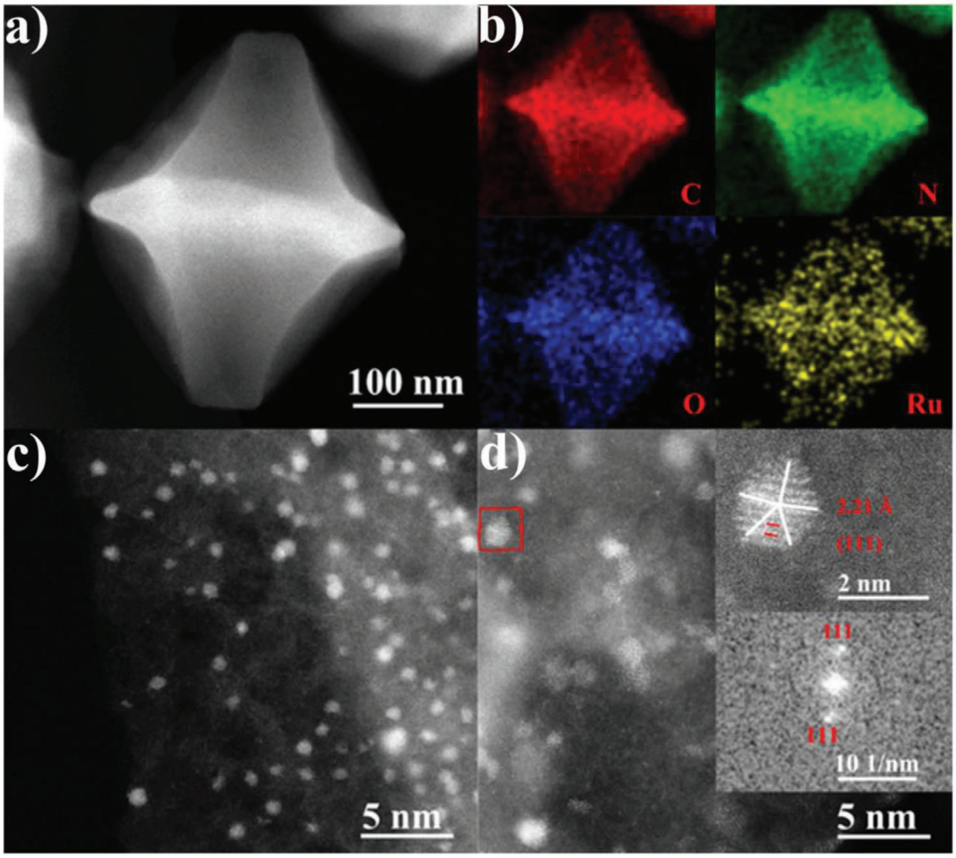

Figure 2. Characterization of Ru-3 a) HAADF-STEM images, b) elemental mapping images, c) magnified HADDF-STEM image, d) magnified HADDF-STEM images, and the FFT pattern of the region signed by red frame.

In this work, for the first time, ultrafine fcc Ru NCs with the size around 1 nm were synthesized by immobilizing Ru aggregate formed in the early stage of crystallization process into in situ generated NDPC. By further increasing the Ru concentration of the MTV MOF, it could be found that the structures of Ru NCs transform from fcc to hcp phase (Figure S21, Supporting Information). This shift in the phase can be confirmed by the shift of lattice constant, which shifts to ≈2.06 Å, corresponding to the lattice spacing of (101) in hcp Ru NCs. The transformation of the crystal phase also matches well with the FFT pattern and the PXRD results. As shown in Figure S22 (Supporting Information), the PXRD patterns of Ru-1a, Ru-1b, and Ru-2 all show a distinctly broad peak at 24.1°, which can be attributed to the (002) crystal plane of graphite carbon.[50] No obvious characteristic peaks of Ru NCs can be observed due to ultrafine size of these Ru-species in the support. These findings are consistent with the HAADF-STEM results. As the proportion of Ru–L increases in these Ru–MOFs, the Ru concentration of the MTV MOF also gradually increases. Thus, the size of the Ru NCs gradually increases. For Ru-3, two very weak diffraction peaks can be detected at 40.92° and 47.81° under slow scan conditions, corresponding to the lattice spacing of (111) and (200) in fcc Ru NCs (Figure S23, Supporting Information). For Ru-4, the diffraction peaks of Ru NCs were well directed in the Ru hcp crystal structure, indicating the transformation of the Ru NCs from the fcc phase to hcp phase with the increase of Ru concentration in the solid solution. This transformation of the crystal phase was also confirmed by the FFT patterns (Figure S21, Supporting Information) and molecular dynamics simulations. As a result, different Ru concentrations of the MTV MOF were determined to play a significant role in the isolation of ultrafine fcc Ru NCs. It also has a great influence on the size and structure of final products.

To further confirm the chemical composition on the surface of these Ru-species, energy dispersive X-ray spectroscopy (XPS) was utilized to again support the simultaneous presence of Ru, N, C, and O in the Ru-1–4 samples (Figure S24, Supporting Information). The C—N peak at 286.5 eV was clearly recorded in the C 1s spectra of Ru-1–4 (**Figure 3**b; and Figure S25, Supporting Information). In the N 1s spectrum of isolated NDPC, three peaks at 398.4, 400.1, and 401.1 eV were designated as pyridinic N, pyrrolic N, and graphitic N, respectively. Pyrrolic N was determined to be the main component in the sample (Figure S26, Supporting Information).[35] Compared to NDPC, the peak at 400.1 eV, related to pyrrolic N in the Ru-1–4 samples, shifts to higher energies after loading the Ru centers in the sample (Figure 3a; and Figure S26, Supporting Information). No obvious shift can be detected for the corresponding C peaks (Figure 3b). These results reveal the coordination of the pyrrolic N with Ru centers in Ru-1–4 samples. These XPS results indicate that the Ru–NCs and the SAs are encapsulated in the NDPC via the Ru–N coordination modes.[51] As shown

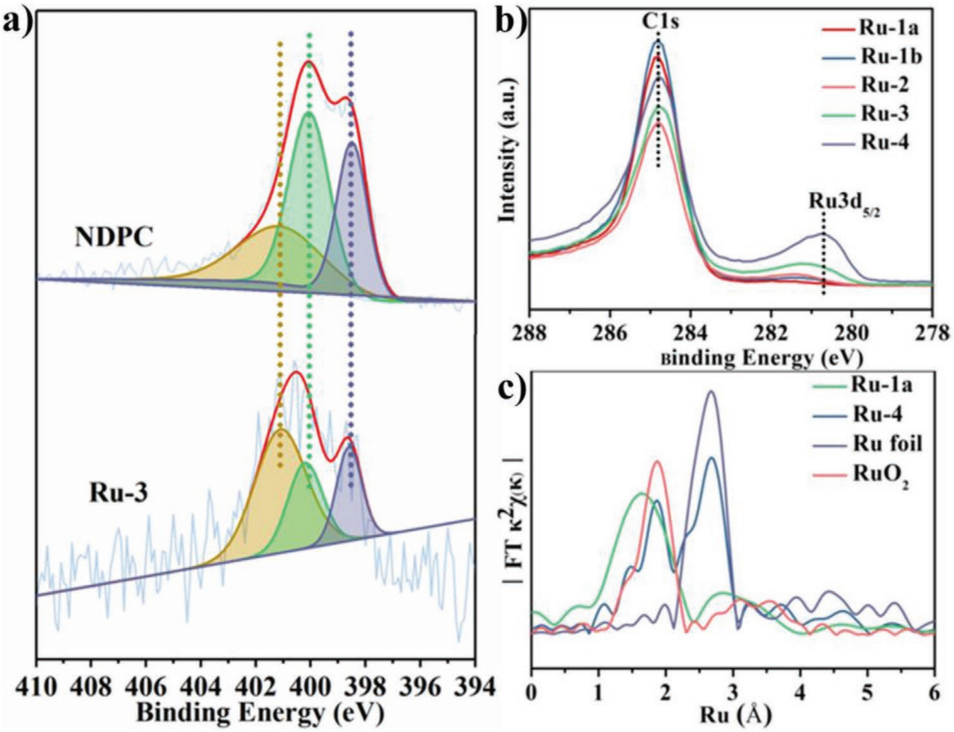

Figure 3. XPS spectra for a) N 1s in NDPC and Ru-3 and b) Ru $3d_{5/2}$ and C 1s in Ru-1–4, c) R-space EXAFS spectra for Ru-1a, Ru-4, Ru foil, and RuO_2.

in Figure 3b; and Figure S27 (Supporting Information), the average Ru valence decreased from +3 to ≈0 when the size of the Ru NCs gradually increased from SA, sub-nm to 2.16 nm NC. For Ru-1a, only Ru^{3+} $3d_{5/2}$ was detected in the SA catalyst, corresponding to the valence of SA Ru centers. This was further confirmed by the X-ray absorption near edge structure (XANES) analysis (Figure S28, Supporting Information). The Ru peaks at 280.2, 280.8, and 281.1 eV in the Ru-4 sample could be attributed to the Ru^0 $3d_{5/2}$, Ru^{2+} $3d_{5/2}$, and Ru^{3+} $3d_{5/2}$, respectively.[52]

2.2. XANES and EXAFS Measurements

XANES and EXAFS measurements were performed to obtain electronic and local coordination structural information. As shown in Figure S28 (Supporting Information), the absorption edge energy of Ru-1a was shown to exhibit an identical profile with that of $Ru(acac)_3$ in the edge range of 22 100 and 22 130 eV. These results revealed that the oxidation state of Ru in the Ru-1a sample was ≈+3, similar to that observed in $Ru(acac)_3$. Ru-1b also exhibited a similar absorption edge energy profile with that of $Ru(acac)_3$, but showed a slightly negative shift compared to that of the Ru-1a sample. These observations indicated that a lower average valence state of the Ru center was observed in Ru-1b as compared to the one seen in Ru-1a. In comparison, the energy absorption edge for both of Ru-3 and Ru-4 was much closer to that of Ru foil. This indicated the low valence of Ru in Ru-3 and Ru-4. This was especially apparent for the Ru-4 sample. These observations agree well with the aforementioned XPS results (Figure 3b; and Figure S27, Supporting Information). As shown in Figure 3c; and Figure S29 (Supporting Information), a prominent peak at ≈1.95 Å for the Ru-1a sample and ≈2.00 Å for the Ru-1b to Ru-4 samples were observed in all the FT-EXAFS curves. These peaks were mainly assigned to the scattering of the Ru–N coordination. This was confirmed by the XPS results and the pristine Ru–N coordination mode observed in the UiO structure.[50] For Ru-1a, no scattering from metallic Ru—Ru was discernible, revealing the atomic dispersion of isolated Ru centers on the NDPC. These results further supported the HAADF-STEM observations (Figure 1c). For Ru-4, a peak located at ≈2.6–2.7 Å was observed, implying the presence of Ru—Ru (Ru^0) metallic bonds. However, the Ru—Ru metal bond in Ru-1–3 cannot be obviously observed in the XANES curves. To further obtain the structure parameters, we conducted a least-squares EXAFS fitting (Figure S29, Supporting Information). As shown in Table S2 (Supporting Information), the FT-EXAFS results show the coordination number of ≈5 for each SA Ru center to the N donors in Ru-1a to Ru-3. This analysis included a contribution of Ru—Ru in Ru-1b to Ru-3. The low average coordination number of Ru—Ru in the sample is due to its minor fraction and/or the ultrafine size of the samples, confirming the HAADF-STEM results (Figure S12, Supporting Information). By further increasing the NC size, the metallic Ru—Ru bonds with a coordination number of 3–4 could be obtained in Ru-4, revealing that the surface Ru centers decrease in concentration with the increase of the fraction of NCs and/or the size of NCs. These results were also confirmed by the increase of the ratio of graphitic N to pyrrolic N from Ru-1 to Ru-4, where pyrrolic N was determined to be the primary contribution for the coordination of the Ru centers (Figure S26, Supporting Information).

2.3. Molecular Dynamics Simulations

To further study the aggregation mechanism of these ultrafine NCs, serials molecular dynamics simulations were carried out to simulate the transformation of Ru species from ordered Ru coordination centers in the MTV MOF to Ru SAs and Ru NCs. Compared with the stable structure at room temperature, when Ru–MOF was heated to 600 and 700 °C, the backbone structure of Ru–MOF was destroyed. Meanwhile, 30 and 41 Ru atoms diffused outside the framework when heated Ru–MOF-1 at 600 and 700 °C, respectively. This observation matches well with the decomposition of Ru–MOF during the pyrolysis, and indicate that Ru atoms can move freely throughout the Ru–MOF and the mobility of Ru atoms at 700 °C is higher than that at 600 °C (Figure S30, Supporting Information). Hence, all followed molecular dynamics simulations were carried out only based on free Ru atoms.

To demonstrate the formation of Ru NCs from Ru SAs when increase the pyrolysis temperature from 600 to 700 °C, the assembly process was calculated with molecular dynamics simulation. As shown in **Figure 4**, the evolution processes for Ru-1b (19 atoms), Ru-2 (55 atoms), Ru-3 (87 atoms), and Ru-4 (369 atoms) start from disorder state (a1–d1 in Figure 4). And then, the atoms nucleate into ultrafine clusters as nuclei within 200 ps (a2–d2), and these clusters assemble to increase in a short time (a3–d3). Finally, these SAs assemble into the NCs and reach the equilibrium state (a4–d4). The fcc pattern can be observed on these final snapshots (a5–d5). Figure 4e is the radial distribution function (rdf) of Ru atoms for the Ru NCs. Ru particles usually have both fcc and hcp lattice face. The distances of Ru atoms are 0.34 and 0.40 nm on fcc and hcp faces, respectively. The peak width change was utilized to demonstrate how Ru particles were derivate from the standard crystalline structure. The larger change of peak shape at hcp position means the particle loses hcp structure. Compared with that of standard NPs (Figure S31, Supporting Information), the rdf of these four systems illustrates that the Ru-1b, Ru-2, and Ru-3 have more ratio of atoms in fcc state than that of Ru-4. Moreover, the potential energy also illustrates the assembly process with the driven force of energy minimization. As shown in Figure S32 (Supporting Information), the simulated curves all possess of a quick decrease at the first region, and the assembly process reaches the platform after 3000 ps. These results reveal the decrease of potential energy during the nucleation process. The averaged potential energy for every atom illustrates that Ru-4 has the lowest energy among all the four systems, which means, Ru-4 has more atoms in hcp pattern. The simulated aggregation procedure matches well with experimental data and demonstrates that Ru centers tend to preferentially aggregate from SAs to ultrafine fcc NCs during the initial aggregation, and eventually transfer from fcc NCs to hcp NCs with a lower energy at higher pyrolysis temperature and Ru concentration. The preferential aggregation from SAs to fcc NCs can supply clear nucleation stage for the formation of the Ru fcc crystal nucleus, thus providing the opportunity for isolating ultrafine fcc Ru NCs with in situ formed supports.

2.4. Methanolytic Dehydrogenation of AB

For the chemical H_2 storage, the AB is very promising for industrial H_2 storage. The exploration of highly efficient catalysts represents a key step in releasing H_2 timely and efficiently by methanolysis of AB, however it still a great challenge for large-scale applications since most of the current high-efficiency catalysts are precious metal catalysts. In this field, development of nonprecious metal catalysts or exploring efficient catalysts with ultra-low loading of precious metal will be a promising way for achieving large-scale applications of this H_2 production system. In this work, these Ru NCs with low Ru content can be used as heterogeneous catalysts to efficiently drive the methanolysis of AB. The reaction was initiated by the introduction of AB into

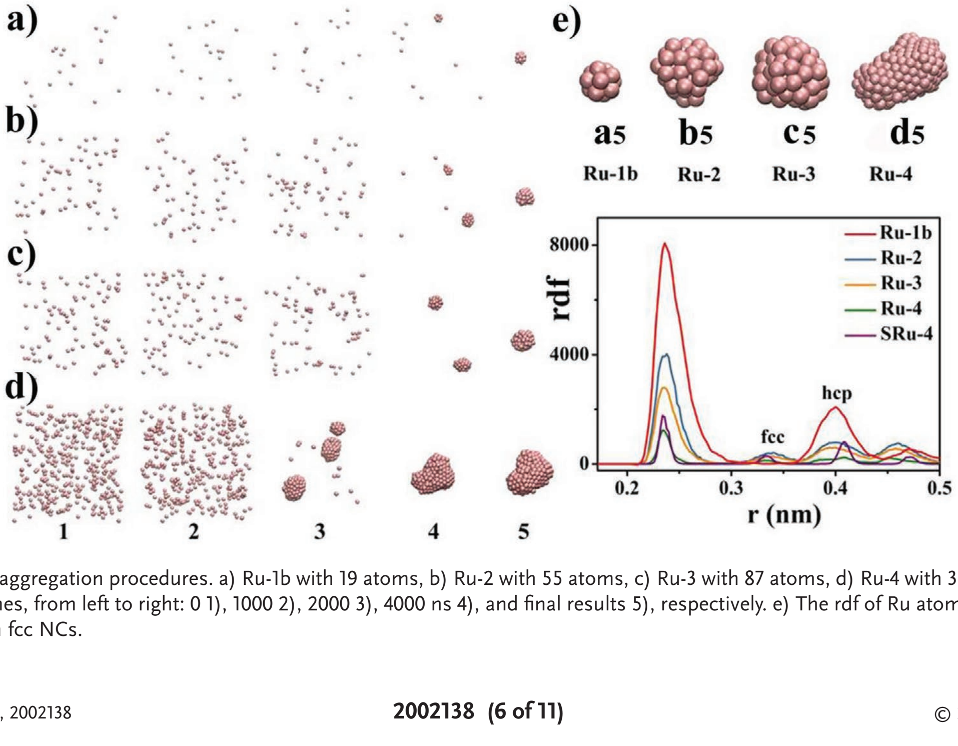

Figure 4. Simulated aggregation procedures. a) Ru-1b with 19 atoms, b) Ru-2 with 55 atoms, c) Ru-3 with 87 atoms, d) Ru-4 with 369 atoms at different simulation time frames, from left to right: 0 1), 1000 2), 2000 3), 4000 ns 4), and final results 5), respectively. e) The rdf of Ru atoms for the NCs, SRu-4 for standard 2.16 nm fcc NCs.

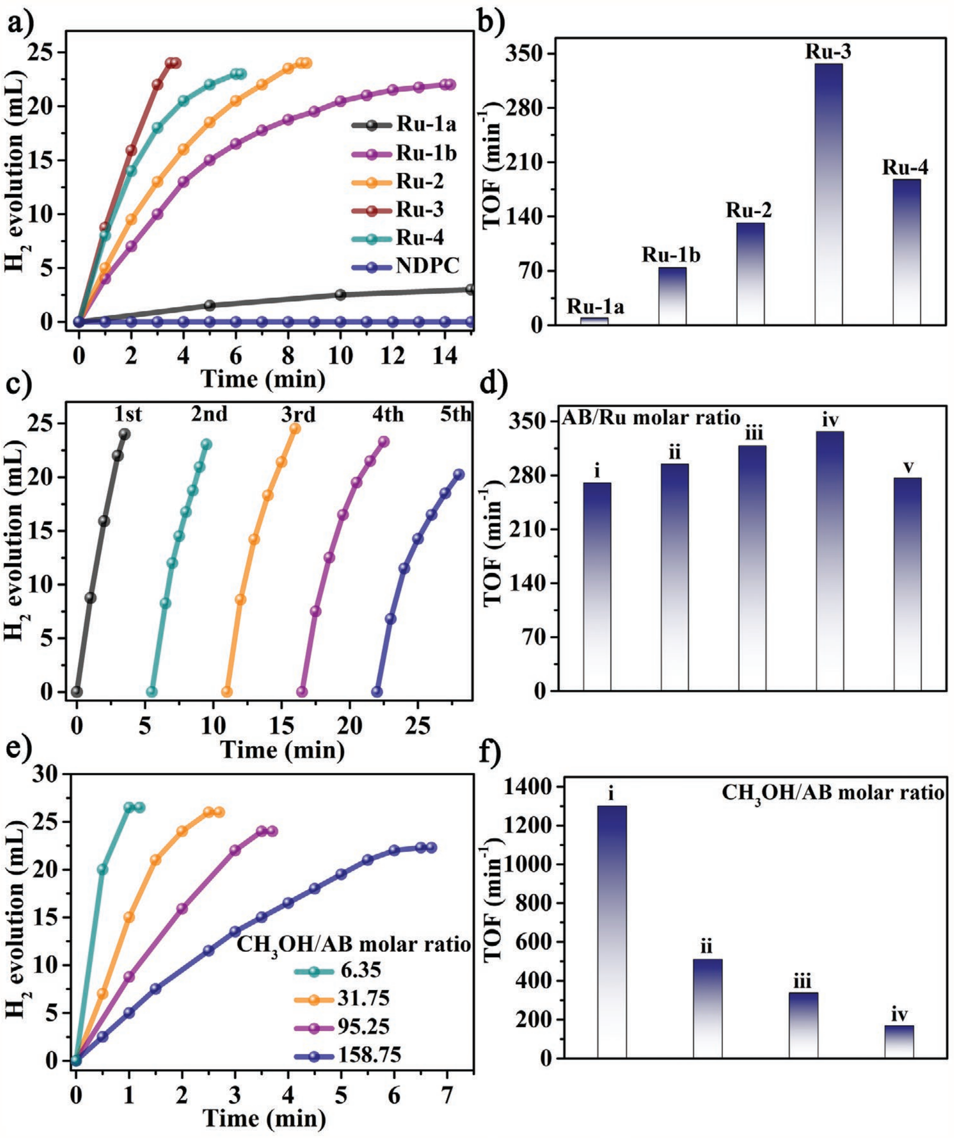

Figure 5. Catalytic performance. a) Time-course plots of H_2 generation for AB methanolysis; b) TOF values of Ru-1–4; c) recycle experiments with Ru-3 as catalyst with AB/Ru molar ratio of 4.67×10^2; d) TOF values of Ru-3 catalyst with different AB/Ru molar ratios (25 °C, CH_3OH/AB molar ratio = 95.25), i) 10.90×10^2, ii) 7.43×10^2, iii) 6.29×10^2, iv) 4.67×10^2, v) 3.27×10^2; e) Time-course plots of H_2 generation and f) TOF values of Ru-3 catalyst with different CH_3OH/AB molar ratio (25 °C, AB/Ru molar ratio = 4.67×10^2), i) 6.35, ii) 31.75, iii) 95.25, iv) 158.75.

a reaction flask containing Ru NC catalysts with vigorous stirring at room temperature (25 °C). The amount of H_2 produced in AB methanolysis was collected and measured through displacement in a water-filled burette. As shown in **Figure 5**, AB can successfully undergo methanolysis to produce H_2 in the presence of these Ru NC catalysts and without any byproducts forming during the reaction (Figures S33–S36, Supporting Information). A series of experiments with different amounts of NC catalysts with a controlled amount of AB catalysts was performed, and related results demonstrate that the hydrogen-generating rates were highly dependent upon the size of the NCs (Figure 5a; and Figure S37, Supporting Information). However, it was also shown that there is less dependence on the AB/Ru molar ratio (Figure 5d; and Figure S38, Supporting Information). It can be clearly observed that the hydrogen release rate notably increases from Ru-1a to Ru-3, and decreases for Ru-4 when controlling equal AB/Ru molar ratio of 4.67×10^2. The TOF decreased from 336.5 min^{-1} of Ru-3 to 73.97 min^{-1} of Ru-1b (**Table 1**) with the decrease of the size of the NCs. This can be further confirmed by the control experiments with Ru-1a as the catalyst, where SA Ru centers possess very low activity toward the methanolytic dehydrogenation of AB. Under these evaluation conditions, this 1.33 nm Ru NC can afford an overall hydrogen generation rate of 81.63 mL min^{-1} $mg_{Ru}{}^{-1}$ with a TOF as high as 336.5 min^{-1}. This is a record-high value among all the reported catalysts (Table 1). However, when the Ru content was increased to 4.01%, the fcc Ru NCs were transformed into hcp phase with a size of 2.16 nm. This material has a much lower catalytic activity compared to that of the Ru-3 with a TOF of 187.66 min^{-1} (Figure 5b). ICP-MS analysis confirmed that the

Table 1. Catalytic activities of the catalysts for methanolytic dehydrogenation of AB.

Entry	Catalyst	Temperature [°C]	AB/M molar ratio [$\times 10^2$]	TOF [min^{-1}]	Reference
1	Ru-1a	25	4.42	2.2	This work
2	Ru-1b	25	4.48	74.0	This work
3	Ru-2	25	4.44	131.8	This work
4	Ru-3	25	4.67	336.5	This work
5	Ru-4	25	4.66	187.7	This work
6	Ru NPs@PCC-2-homo	25	2.86	304.4	[29]
7	Ru NPs@PVP	25	2.86	38.1	[29]
8	HPRhS	25	2.06	296.1	[60]
9	Rh(0)/nanoCeO$_2$	25	4.23	144.0	[61]
10	Rh/nanoSiO$_2$	25	4.08	168.0	[63]
11	Rh/CC3-R-homo	25	0.50	215.3	[31]
12	Rh/CC3-R-hetero	25	0.50	65.5	[31]
13	Rh/P(triaz)	25	1.00	260.0	[64]
14	Rh/nanoHAP	25	4.93	147.0	[57]
15	Ru/MMT	25	3.33	118.1	[58]
16	Ru/graphene	25	3.33	99.4	[59]
17	Pd/C	25	0.5	2.4	This work

loading amount of Ru in Ru-3 (2.40%) is much lower than that of Ru-4 (4.01%), and the proportion of SAs Ru in Ru-3 is much higher than that in Ru-4 confirmed by HAADF-STEM and FT-EXAFS measurements. In addition, the SA Ru centers exhibited a much lower activity toward the methanolytic dehydrogenation of AB. As a result, it can be concluded that the catalytic activity of fcc NCs with more exposed active sites is much higher than that of the hcp Ru variant.

Based on above results, it can be concluded that Ru-3 represents the most active catalysts among these reported samples. Therefore, the Ru-3 was used as a model catalyst to optimize the reaction conditions. As shown in Figure 5e; and Figure S39 (Supporting Information), the catalytic reaction was performed at different reaction temperatures of 25, 30, 35, and 40 °C with Ru-3 as the catalyst. It could be found that the reaction shows higher catalytic activity at a higher temperature, which was consistent with the reported results.[53] Further, methanol/AB molar ratios with 6.35, 31.75, 95.25, and 158.75 were further used to perform the catalytic reaction. When the methanol/AB molar ratio is 6.35, the TOF can reach as high as 1300.53 min^{-1} (Figure 5f), ≈4 times higher than that with the ratio of 95.25, representing the most efficient catalytic system among these catalytic systems. To confirm whether the Zr element affects the catalytic performance, the blank NDPC obtained from isolated UiO–MOF without any Ru spieces was used as the catalyst. ICP analysis reveals that some Zr element remains in the NDPC. As shown in Figure 5a, only trace amount of H_2 can be detected, indicating that the NDPC did not have obvious influence on the catalytic performance. For Ru-1a, a Ru SA catalyst with similar Zr content to Ru-3 also shows very low catalytic activity (Figure 5a). All these results confirm that the fcc Ru NC was the really catalytic active center for the methanolysis of AB, and Zr element do not have obvious influence on the catalytic performance.

The catalytic process of the methanolysis of AB occurs on the surface of metal nanomaterials forming activated composite species via the interaction between AB molecules and surface metal centers. The first step is the formation of activated composites, which were then attacked by CH_3OH, resulting in synergistic cleavage of B—N bond and methanolysis of the resulting BH_3^-intermediate to yield $B(OCH_3)_4^-$ and H_2.[54] In this work, these ultrafine Ru NCs exhibit prominent size and geometric effects to their functionalities, where fcc Ru NCs with the diameter of 1.33 nm exhibit record-high catalytic activity for the methanolysis of AB with a turnover frequency of 336.5 min^{-1} at ambient temperatures. It can be proposed that the suitable metal particle size, structure, and geometric effects of NCs all play important roles in the improvement of the catalytic activity. 1) The aggregation of Ru metal centers into ultrafine NCs facilitates direct contact between the substrate and the Ru metal centers. The methanolysis of AB, generating H_2, is a multiactive site synergetic catalytic reaction.[55–61] When compared to SA, the Ru-1a–3 catalysts all have characteristics of multiple adjacent active sites. The conversion of adsorbed substrates was also carried out simultaneously at several active sites, increasing the rate of the catalytic reaction.[30] EXAFS results also show a higher coordination number (CN) for Ru—Ru in the Ru-3 sample than that of the Ru-1 samples. 2) The reaction is also facilitated by less interaction between the Ru NCs and the NDPC supports. The interaction between the metal NCs and the support should be weakened with increasing the size of Ru NCs in the catalyst. This result can be confirmed by XPS characterization (Figure S26, Supporting Information), where the percentage of N coordinated with Ru centers decreases gradually with increasing concentration of the Ru in the MTV MOF. Thus, the binding ability between active species on the metal surface and the support is reduced, leading to higher catalytic activity. 3) The structure and geometric effects of the NCs both play important roles in improving the catalytic activity. With the increased concentration of Ru in the samples, the Ru centers tend to form more stable hcp Ru NCs. This is seen in the Ru-4 sample with a slightly larger size and lower facial index exposed than that of the (111) and (200) face in fcc Ru NCs.[29,62] As well known, Ru centers on the NC surface with higher lattice index (fcc) have lower coordination number, which leads to stronger binding of AB with lower energy. As a result, the fcc Ru NCs show a much better performance in the methanolysis reaction of AB than that of hcp Ru NCs.

To verify that hydrogen production over Ru NCs was generated via the methanolysis of AB, we conducted a series of control experiments. When the reaction proceeded by adding only AB to methanol in the absence of catalyst or using isolated NDPC as catalyst, the hydrogen cannot be obviously detected (Figure 5a; and Figure S40, Supporting Information). Therefore, it is concluded that the presence of Ru NCs is necessary for the hydrogen production by AB methanolysis. Further, after the catalytic reaction, Ru-1a and Ru-3 were washed several times with methanol and dried in a vacuum oven at 60 °C for recycle experiments. The recycle experiments show only a slight loss of the performance after five cycles of tests (Figure 5c). After completing the catalytic experiments, TEM and HRTEM studies show that Ru-3 still retains its pristine morphology, no obvious aggregation of the Ru NCs could be observed (Figure S41, Supporting Information). EDS results showed that the Ru loading ratio also maintained the same with that before the catalysis (Figure S42, Supporting Information). No Ru nanoparticles can be observed on the TEM images of Ru-1a after the catalytic reaction (Figure S43, Supporting Information). PXRD measurement reveals that no obvious peaks of the Ru particles could be detected of Ru-3 (Figure S44, Supporting Information). All these results confirm the good stability of the catalyst in the catalytic process.

3. Conclusion

In conclusion, we have developed an efficient strategy for controllable construction of ultrafine fcc Ru NCs by mimicking the liquid-phase crystal growth process via the pyrolysis of a solid solution. In this method, the Ru centers are uniformly dispersed into the solid solution during the assembly and crystallization process of the MTV MOF, and the Ru concentrations were adjusted by altering the loading amount of Ru–L ligand. The aggregation process of Ru centers can be facilely controlled via adjusting the pyrolysis temperature and Ru concentration in the MTV MOF, further controlling the crystalline phase and size of the Ru NCs. The successful synthesis of the SA catalyst and a series of Ru NCs from sub-nm to 2.16 nm confirmed that the aggregation and nucleation of the metal cations does occur in the solid solution in the initial step of the fcc crystal nucleus into the in situ formed stabilizers. A detail study of the catalytic activity revealed that these ultrafine Ru NCs exhibit prominent size and geometric effects. 1.33 nm fcc Ru NC sample exhibits a record-high catalytic activity for the methanolysis of AB at ambient temperature with high stability. This work highlights an efficient method to synthesize ultrafine metal NCs by the simulation of liquid-phase crystal growth processes with in situ formation of a strong stabilizer to stabilize ultrafine crystal nucleus formed during the initial nucleation.

4. Experimental Section

Materials and Characterization: All chemicals were commercially available and used without further purification. *N*,*N*-dimethylfor-mamide (DMF), methanol (CH_3OH), zirconium chloride ($ZrCl_4$), glacial acetic acid (HAc), hydrofluoric acid solution (HF 40%), and ruthenium(III) chloride hydrate ($RuCl_3$•$3H_2O$), 4,4-biphenyldicarboxylic acid ($C_{14}H_{10}O_4$) were obtained from Shanghai Chemical Reagents, China. Deionized water was used in all experiments. $Ru(H_2bpydc)(bpy)_2Cl_2$ (Ru–L) and $Ru(bpy)_2Cl_2$, were synthesized according to literature methods.[48] PXRD data were collected by a Smart X-ray diffractometer (SmartLab 9 KW, Rigaku, Japan). EDS elemental mapping images and HAADF-STEM images were taken using Aberration-corrected scanning transmission electron microscope (Titan Themis Cubed G260-300, FEI, America). TEM images were performed on transmission electron microscope (Tecnai G2 Spirit TWIN, FEI, America). Ru content was determined by ICP-MS) iCAP RQ, Germany). XPS was operated on an ESCALAB250Xi (Thermo, England). The X-ray absorption fine structure (XAFS) spectra at Ru K (E_0 = 22 117 eV) edge was performed at BL14W1 beamline of Shanghai Synchrotron Radiation Facility operated at 3.5 GeV under "top-up" mode with a constant current of 240 mA. The XAFS data were recorded under fluorescence mode with a 7-element Ge solid state detector. The energy was calibrated accordingly to the absorption edge of pure Ru foil. Athena and Artemis codes were used to extract the data and fit the profiles. For the XANES part, the experimental absorption coefficients as function of energies μ(E) were processed by background subtraction and normalization procedures, and reported as "normalized absorption" with E_0 = 22 117 eV for all the measured samples and references (Ru foil for Ru^0, $Ru(acac)_3$ for Ru^{3+}, and RuO_2 for Ru^{4+}). For the EXAFS part, the Fourier transformed (FT) data in R space were analyzed by applying first-shell approximate (assuming that each Ru center is coordinated with four N atoms) and metallic Ru (fcc structure; space group #: 225) models for Ru–N and Ru—Ru contributions, respectively. The passive electron factors, S_0^2, were determined as 0.84 by fitting the experimental data on Ru foil and fixing the coordination number (CN) of Ru—Ru to be 6+6, and then fixed for further analysis of the measured samples. The parameters describing the electronic properties (e.g., correction to the photoelectron energy origin, E_0) and local structure environment parameters including CN, bond distance (R), and Debye–Waller factor (σ^2) around the absorbing atoms were varied during the fit process. The fitted ranges for k space were selected to be k = 3–11 Å^{-1}. The R-factor of each fit was lower than 3%.

Synthesis of UiO-67 MOF: UiO-67 was synthesized according to literature methods.[48] The typical procedure was as follows: UiO-67 MOF was synthesized by the reaction of $ZrCl_4$ (10.0 mg, 0.043 mmol) and H_2bpdc (10.4 mg, 0.043 mmol) in 1.5 mL DMF. Then, 85 μL glacial acetic acid was added to the vial and was then heated at 100 °C for 24 h. After cooling, the resulting solids were isolated by centrifugation and washed with DMF and CH_3OH repeatedly before drying under vacuum.

Synthesis of Ru–MOF-1-5: Ru–MOF-1 was synthesized through the reaction of $ZrCl_4$ (10.0 mg, 0.043 mmol), H_2bpdc (10.1 mg), Ru–L (0.74 mg), and 85 μL glacial acetic acid in 1.5 mL DMF under solvothermal conditions at 100 °C for 24 h. After cooling, the resulting solids were isolated by centrifugation, and washed with DMF and CH_3OH repeatedly before drying under vacuum. The synthetic conditions of Ru–MOF-2-4 were similar to that of Ru–MOF-1, with the main exception being variations in the amounts of H_2bpdc (10.0 mg for Ru–MOF-2; 9.4 mg for Ru–MOF-3; 8.7 mg for Ru–MOF-4) and Ru–L (1.0 mg for Ru–MOF-2; 2.8 mg for Ru–MOF-3; 5.1 mg for Ru–MOF-4). In the synthesis of Ru–MOF-1-4, the molar ratios of H_2bpdc/Ru–L were 40: 1, 30: 1, 10: 1, 5: 1, respectively. The synthesis of Ru–MOF-5 was also similar to that of Ru–MOF-1, with the exception that $RuCl_3$•$3H_2O$ (1.27 mg) was used instead of Ru–L in the synthesis of Ru–MOF-1.

Synthesis of ZrO_2–Ru-1-5 and Ru-1-5: The powder of Ru–MOF-1-5 was placed in a tube furnace and heated to 600 °C for Ru-1a and 700 °C for Ru-1b-Ru-5 with a heating rate of 2 °C min^{-1} under argon flow. This procedure was followed by another 3 h treatment at a same temperature under argon atmosphere. After cooling to room temperature, black powders, ZrO_2–Ru-1-5, were collected and were further dispersed in 0.1 M HF aqueous solution (15 mL) for 2 h. The resulting turbid liquid was centrifuged at 11 000 rpm for 5 min. Subsequently, the resultant product was washed with methanol and H_2O (v/v = 1: 4) three times and dried under vacuum at 100 °C for further use. The black powder of isolated NDPC was synthesized with a similar procedure by the thermal treatment of UiO-67 MOF at 700 °C under argon flow.

Catalytic Activity: The powder of Ru-1-5 is activated at 250 °C for 2 h with a heating rate of 5 °C min^{-1} under an atmosphere of 5% H_2 and 95% N_2 before the catalytic reaction. The activated Ru–NC catalyst was placed in a two-necked round-bottomed flask (30 mL), which was placed in a water bath under ambient atmosphere. A gas burette filled with water was connected to the reaction flask to measure the volume of hydrogen generated. The solid Ru–NC catalysts (52.2, 30.2, 15.5, 3.5, 2.1 mg for Ru-1a to Ru-4, respectively) and 1.5 mL methanol were added the flask. The reaction was started when a methanol solution containing 12 mg AB was added into the solution. The gas and liquid products were identified by gas chromatography (Figure S30, Supporting Information). The amount of the produced H_2 was monitored by recording the displacement of water in the gas burette. The reaction was completed when there was no more gas generation.

TOF is based on the amount of Ru atoms, which was calculated from the equation below

$$\mathrm{TOF} = V\mathrm{H}_2/(V_\mathrm{m}\cdot n_\mathrm{Ru}\cdot t) \quad (1)$$

$V\mathrm{H}_2$ is the total volume of generated H_2,V_m is calculated by RT/Patm (Patm is 101.325 kPa, R is 8.3145 m^3 Pa mol^{-1} K^{-1}, and T is 298 K), n_Ru is the total mole number of Ru atoms in catalyst, and t is the completion time of the reaction in minute.

Supporting Information

Supporting Information is available from the Wiley Online Library or from the author.

Acknowledgements

Y.-W. and J.-L. contributed equally to this work. This work was supported the National Natural Science Foundation of China (Nos. 21722104, 21671032, 21931007, and 21971190), and Natural Science Foundation of Tianjin City of China (No. 18JCJQJC47700) and 111 project of China (No. D17003).

Conflict of Interest

The authors declare no conflict of interest.

Keywords

dehydrogenation, fcc Ru, nanoclusters, nucleation, single atoms

Received: June 30, 2020
Revised: September 14, 2020

---

[1] J. N. Tiwari, A. M. Harzandi, M. Ha, S. Sultan, C. W. Myung, H. J. Park, D. Y. Kim, P. Thangavel, A. N. Singh, P. Sharma, S. S. Chandrasekaran, F. Salehnia, J. W. Jang, H. S. Shin, Z. Lee, K. S. Kim, *Adv. Energy Mater.* **2019**, *9*, 1900931.
[2] X. C. Yang, J. K. Sun, M. Kitta, H. Pang, Q. Xu, *Nat. Catal.* **2018**, *1*, 214.
[3] L. C. Liu, A. Corma, *Chem. Rev.* **2018**, *118*, 4981.
[4] S. F. Ji, Y. J. Chen, Q. Fu, Y. F. Chen, J. C. Dong, W. X. Chen, Z. Li, Y. Wang, L. Gu, W. He, C. Chen, Q. Peng, Y. Huang, X. F. Duan, D. S. Wang, C. Draxl, Y. D. Li, *J. Am. Chem. Soc.* **2017**, *139*, 9795.
[5] Y. Fang, Z. F. Xiao, J. L. Li, C. Lollar, L. J. Liu, X. Z. Lian, S. Yuan, S. Banerjee, P. Zhang, H. C. Zhou, *Angew. Chem., Int. Ed.* **2018**, *57*, 5283.
[6] D. Kim, J. Resasco, Y. Yu, A. M. Asiri, P. D. Yang, *Nat. Commun.* **2014**, *5*, 4948.
[7] J. Liu, W. Shi, B. Ni, Y. Yang, S. Li, J. Zhuang, X. Wang, *Nat. Chem.* **2019**, *11*, 839.
[8] H. G. Wang, X. K. Gu, X. S. Zheng, H. B. Pan, J. F. Zhu, S. Chen, L. N. Cao, W. X. Li, J. L. Lu, *Sci. Adv.* **2019**, *5*, eaat6413.
[9] W. P. Gao, P. Tieu, C. Addiego, Y. L. Ma, J. B. Wu, X. Q. Pan, *Sci. Adv.* **2019**, *5*, eaau9590.
[10] Z. Q. Niu, N. Becknell, Y. Yu, D. Kim, C. Chen, N. Kornienko, C. A. Somorjai, P. D. Yang, *Nat. Mater.* **2016**, *15*, 1188.
[11] L. Z. Bu, N. Zhang, S. J. Guo, X. Zhang, J. Li, J. L. Yao, T. Wu, G. Lu, J. Y. Ma, D. Su, X. Q. Huang, *Science* **2016**, *354*, 1410.
[12] L. C. Liu, A. Corma, *Trends Chem.* **2020**, *2*, 383.
[13] Q. P. Lu, A. L. Wang, Y. Gong, W. Hao, H. F. Cheng, J. Z. Chen, B. Li, N. L. Yang, W. X. Niu, J. Wang, Y. F. Yu, X. Zhang, Y. Chen, Z. X. Fan, X. J. Wu, J. P. Chen, J. Luo, S. Z. Li, L. Gu, H. Zhang, *Nat. Chem.* **2018**, *10*, 456.
[14] W. H. Lai, Y. X. Wang, Y. Wang, M. H. Wu, J. Z. Wang, H. K. Liu, S. L. Chou, J. Chen, S. X. Dou, *Nat. Chem.* **2019**, *11*, 695.
[15] J. Liu, W. Shi, X. Wang, *J. Am. Chem. Soc.* **2019**, *141*, 18754.
[16] Y. C. Yao, D. S. He, Y. Lin, X. Q. Feng, X. Wang, P. Q. Yin, X. Hong, G. Zhou, Y. E. Wu, Y. D. Li, *Angew. Chem., Int. Ed.* **2016**, *55*, 5501.
[17] J. Mahmood, F. Li, S. M. Jung, M. S. Okyay, I. Ahmad, S. J. Kim, N. Park, H. Y. Jeong, J. B. Baek, *Nat. Nanotechnol.* **2017**, *12*, 441.
[18] Y. Zheng, Y. Jiao, Y. H. Zhu, L. H. Li, Y. Han, Y. Chen, M. Jaroniec, S. Z. Qiao, *J. Am. Chem. Soc.* **2016**, *138*, 16174.
[19] A. X. Yin, W. C. Liu, J. Ke, W. Zhu, J. Gu, Y. W. Zhang, C. Yan, *J. Am. Chem. Soc.* **2012**, *134*, 20479.
[20] A. M. Harzandi, S. Shadman, M. Ha, Ch. W. Myung, D. Y. Kim, H. J. Park, S. Sultan, W. S. Noh, W. Lee, P. Thangavel, W. J. Byun, S. Lee, J. N. Tiwari, T. J. Shin, J. H. Park, Z. Lee, J. S. Lee, K. S. Kim, *Appl. Catal., B* **2020**, *270*, 118896.
[21] Y. Q. Deng, L. J. Yang, Y. K. Wang, L. L. Zeng, J. Y. Yu, B. Chen, X. L. Zhang, W. J. Zhou, *Chin. Chem. Lett.* **2020**, https://doi.org/10.1016/j.cclet.2020.03.076.
[22] H. H. Ye, Q. X. Wang, M. Catalano, N. Lu, J. Vermeylen, M. J. Kim, Y. Z. Liu, Y. G. Sun, X. H. Xia, *Nano Lett.* **2016**, *16*, 2812.
[23] L. Huang, X. P. Zhang, Q. Q. Wang, Y. J. Han, Y. X. Fang, S. J. Dong, *J. Am. Chem. Soc.* **2018**, *140*, 1142.
[24] H. Y. Ma, C. Z. Na, *ACS Catal.* **2015**, *5*, 1726.
[25] L. Gloag, T. M. Benedetti, S. Cheong, Y. B. Li, X. H. Chan, L. Lacroix, S. L. Y. Chang, R. Arenal, I. Florea, H. Barron, A. S. Barnard, A. M. Henning, C. Zhao, W. Schuhmann, J. J. Gooding, R. D. Tilley, *Angew. Chem., Int. Ed.* **2018**, *57*, 10241.
[26] M. Zhao, L. F. Cosme, A. O. Elnabawy, M. Vara, X. Yang, L. T. Roling, M. F. Chi, M. Mavrikakis, Y. N. Xia, *Nano Lett.* **2016**, *16*, 5310.
[27] W. Z. Li, J. X. Liu, J. Gu, W. Zhou, S. Y. Si, R. Yao, Y. Guo, H. Y. Su, C. H. Yan, W. X. Li, Y. W. Zhang, D. Ma, *J. Am. Chem. Soc.* **2017**, *139*, 2267.
[28] K. Kusada, H. Kobayashi, T. Yamamoto, S. Matsumura, N. Sumi, K. Sato, K. Nagaoka, Y. Kubota, H. Kitagawa, *J. Am. Chem. Soc.* **2013**, *135*, 5493.
[29] Y. Fang, J. L. Li, T. Togo, F. Y. Jin, Z. F. Xiao, L. J. Liu, H. Drake, X. Z. Lian, H. C. Zhou, *Chem* **2018**, *4*, 555.
[30] Y. Guo, S. Mei, K. Yuan, D. J. Wang, H. C. Liu, C. H. Yan, Y. W. Zhang, *ACS Catal.* **2018**, *8*, 6203.
[31] J. K. Sun, W. W. Zhan, T. Akita, Q. Xu, *J. Am. Chem. Soc.* **2015**, *137*, 7063.
[32] K. Kusada, H. Kitagawa, *Adv. Mater.* **2016**, *28*, 1129.
[33] M. Zhao, Z. T. Chen, Z. Lyu, Z. D. Hood, M. H. Xie, M. Vara, M. F. Chi, Y. N. Xia, *J. Am. Chem. Soc.* **2019**, *141*, 7028.
[34] L. Gloag, T. M. Benedetti, S. Cheong, C. E. Marjo, J. J. Gooding, R. D. Tilley, *J. Am. Chem. Soc.* **2018**, *140*, 12760.
[35] X. Wang, W. X. Chen, L. Zhang, T. Yao, W. Liu, Y. Lin, H. X. Ju, J. C. Dong, L. R. Zheng, W. S. Yan, X. S. Zheng, Z. J. Li, X. Q. Wang, J. Yang, D. S. He, Y. Wang, Z. X. Deng, Y. E. Wu, Y. D. Li, *J. Am. Chem. Soc.* **2017**, *139*, 9419.
[36] G. D. Li, S. L. Zhao, Y. Zhang, Z. Y. Tang, *Adv. Mater.* **2018**, *30*, 1800702.
[37] T. He, S. M. Chen, B. Ni, Y. Gong, Z. Wu, L. Song, L. Gu, W. P. Hu, X. Wang, *Angew. Chem., Int. Ed.* **2018**, *57*, 3493.
[38] M. Z. Hu, S. Zhao, S. J. Liu, C. Chen, W. X. Chen, W. Zhu, C. Liang, W. C. Cheng, Y. Wang, Y. Yu, Q. Peng, K. B. Zhou, J. Li, Y. D. Li, *Adv. Mater.* **2018**, *30*, 1801878.

[39] S. Ji, Y. Chen, X. Wang, Z. Zhang, D. Wang, Y. Li, *Chem. Rev.* **2020**, https://doi.org/10.1021/acs.chemrev.9b00818.

[40] R. V. Jagadeesh, K. Murugesan, A. S. Alshammari, H. Neumann, M. M. Pohl, J. Radnik, M. Beller, *Science* **2017**, *358*, 326.

[41] L. Y. Chen, R. Luque, Y. W. Li, *Chem. Soc. Rev.* **2017**, *46*, 4614.

[42] Q. L. Zhu, J. Li, Q. Xu, *J. Am. Chem. Soc.* **2013**, *135*, 10210.

[43] Y. Z. Chen, Z. Y. U. Wang, H. W. Wang, J. L. Lu, S. H. Yu, H. L. Jiang, *J. Am. Chem. Soc.* **2017**, *139*, 2035.

[44] F. R. Fortea-Pérez, M. Mon, J. Ferrando-Soria, M. Boronat, A. Leyva-Pérez, A. Corma, J. M. Herrera, D. Osadchii, J. Gascon, D. Armentano, E. Pardo, *Nat. Mater.* **2017**, *16*, 760.

[45] X. F. Lu, L. Yu, J. Zhang, X. W. (David) Lou, *Adv. Mater.* **2019**, *31*, 190069.<./bib>

[46] L. M. Aguirre-Díaz, F. Gándara, M. Iglesias, N. Snejko, E. Gutiérrez-Puebla, M. Á. Monge, *J. Am. Chem. Soc.* **2015**, *137*, 6132.

[47] M. L. Foo, S. Horike, T. Fukushima, Y. Hijikata, Y. Kubota, M. Takataf, S. Kitagawa, *Dalton Trans.* **2012**, *41*, 13791.

[48] C. Wang, Z. G. Xie, K. E. DeKrafft, W. B. Lin, *J. Am. Chem. Soc.* **2011**, *133*, 13445.

[49] B. Lim, M. J. Jiang, J. Tao, P. H. C. Camargo, Y. M. Zhu, Y. N. Xia, *Adv. Funct. Mater.* **2009**, *19*, 189.

[50] Z. G. Geng, Y. Liu, X. D. Kong, P. Li, K. Li, Z. Y. Liu, J. J. Du, M. Shu, R. Si, J. Zeng, *Adv. Mater.* **2018**, *30*, 1803498.

[51] Y. Y. Zhou, L. Zhang, W. Z. Wang, *Nat. Commun.* **2019**, *10*, 506.

[52] E. A. Paoli, F. Masini, R. Frydendal, D. Deiana, C. Schlaup, M. Malizia, T. W. Hansen, S. Horch, I. E. L. Stephens, I. Chorkendorff, *Chem. Sci.* **2015**, *6*, 190.

[53] Q. M. Sun, N. Wang, T. J. Zhang, R. S. Bai, A. Mayoral, P. Zhang, Q. H. Zhang, O. Terasaki, J. H. Yu, *Angew. Chem., Int. Ed.* **2019**, *131*, 18743.

[54] W. W. Zhan, Q. L. Zhu, Q. Xu, *ACS Catal.* **2016**, *6*, 6892.

[55] M. Mahyari, A. Shaabani, *J. Mater. Chem. A* **2014**, *2*, 16652.

[56] C. Y. Peng, L. Kang, S. Cao, Y. Chen, Z. S. Lin, W. F. Fu, *Angew. Chem., Int. Ed.* **2015**, *54*, 15725.

[57] D. Özhava, S. Özkar, *Int. J. Hydrogen Energy* **2015**, *40*, 10491.

[58] H. B. Dai, X. D. Kang, P. Wang, *Int. J. Hydrogen Energy* **2010**, *35*, 10317.

[59] S. G. Peng, J. C. Liu, J. Zhang, F. Y. Wang, *Int. J. Hydrogen Energy* **2015**, *40*, 10856.

[60] H. B. Zou, B. Jin, R. W. Wang, Y. B. Wu, H. Q. Yang, S. L. Qiu, *J. Mater. Chem. A* **2018**, *6*, 24166.

[61] D. Özhava, S. Özkar, *Appl. Catal., B* **2018**, *237*, 1012.

[62] K. Kusada, H. Kobayashi, R. Ikeda, Y. Kubota, M. Takata, S. Toh, T. Yamamoto, S. Matsumura, N. Sumi, K. Sato, K. Nagaoka, H. Kitagawa, *J. Am. Chem. Soc.* **2014**, *136*, 1864.

[63] D. Özhava, S. Özkar, *Appl. Catal., B* **2016**, *181*, 716.

[64] J. K. Sun, Z. Kochovski, W. Y. Zhang, H. Kirmse, Y. Lu, M. Antonietti, J. Y. Yuan, *J. Am. Chem. Soc.* **2017**, *139*, 8971.